Water Vapour Exchange between Atmospheric Boundary Layer and Free Troposphere over Eastern China: Seasonal Characteristics and ENSO Anomaly

Xipeng Jin[1], Xuhui Cai[2*], Xuesong Wang[2], Qianqian Huang[3], Yu Song[2], Ling Kang[2], Hongsheng Zhang[4], Tong Zhu[2]

[1]Collaborative Innovation Center of Atmospheric Environment and Equipment Technology, Jiangsu Key Laboratory of Atmospheric Environment Monitoring and Pollution Control, School of Environmental Science and Engineering, Nanjing University of Information Science & Technology, Nanjing 210044, China
[2]State Key Lab of Environmental Simulation and Pollution Control, College of Environmental Sciences and Engineering, Peking University, Beijing 100871, China
[3]Institute of Urban Meteorology, Beijing 100089, China
[4]Department of Atmospheric and Oceanic Sciences, School of Physics, Peking University, Beijing 100871, China

Correspondence to: Xuhui Cai (E-mail: xhcai@pku.edu.cn)

1 **Abstract.** This study develops a quantitative climatology of water vapour exchange between
2 the atmospheric boundary layer (ABL) and free troposphere (FT) over eastern China. The
3 exchange flux is estimated for January, April, July, and October over 7 years based on a water
4 vapour budget equation using simulated meteorological data. The spatiotemporal
5 characteristics and occurrence mechanism of ABL-FT water vapour exchange and its
6 relationship with ENSO are revealed: (1) The vertical exchange flux varies regionally and
7 seasonally, with downward transport to maintain ABL moisture during winter and autumn in
8 the northern region and persistent output to humidify FT in the southern region, particularly in
9 summer. Additionally, the vertical exchange flux is also topographic dependent. (2) The
10 vertical motion at the ABL top, which is produced by the dynamic forcing of the terrain on
11 synoptic winds, is the dominant mechanism for the water vapour vertical exchange over the
12 long-term average. The evolution of the vertical exchange flux within one-day scale is driven
13 by the ABL diurnal cycle. (3) The interannual variation of water vapour vertical exchange is
14 correlated with ENSO. A triple antiphase distribution with negative-positive-negative
15 anomalies from north to south exists in La Niña years (and vice versa in El Niño years), which
16 corresponds to the spatial pattern of anomalous precipitation. This phenomenon is mainly due
17 to the alteration of vertical velocity and water vapour content at the ABL top varying with
18 ENSO phases. These results provide new insight into understanding the atmospheric water
19 cycle.

20 **Keywords**: Water vapour; atmospheric boundary layer; free troposphere; vertical exchange

1 Introduction

Water vapour is a significant constituent in the atmosphere. It directly participates in fundamental physical processes, including cloud formation, precipitation, severe weather development and atmospheric circulation (Sodemann and Stohl, 2013; Wong et al., 2018; Wypych et al., 2018). Water vapour also affects important chemical reactions, such as providing OH radicals for gaseous photochemical transformations and serving as a medium in secondary aerosol formations (Pilinis et al., 1989; Tabazadeh 2000; Wu et al., 2019). Moreover, the radiation forcing of water vapour accounts for about 2/3 of the total natural greenhouse effect, which plays a vital role in climate feedback (Kiehl and Trenberth, 1997; Harries et al., 2008; Adebiyi et al., 2015).

The distribution of water vapour in the atmospheric system depends on its source and transport processes. In general, water vapour evaporates from the Earth's surface into the atmosphere. From the meridional and zonal view, it presents a transport trend from low latitude to high latitude and from ocean to land. The horizontal transport of water vapour has been widely discussed from multiple scales. Hemispheric-scale atmospheric rivers induce large excursions of high vertically integrated water vapour from the subtropics to high latitudes (Newell et al. 1992; Zhu and Newell 1998; Sodemann and Stohl, 2013). Synoptic-scale moisture flux convergence of extratropical cyclones explains the precipitations and cloud structures over the warm front and cold front (Boutle et al., 2010; Wong et al., 2018). Regional-scale transport processes are widely reported in many areas from water vapour advection and dynamical convergence (Zhou and Yu, 2005; Sun et al., 2010; Gvozdikova and Muller, 2021). However, these studies estimate vertically integrated water vapour through the atmospheric layer (usually from the surface to 300 hPa) or only focused on a certain altitude.

The water vapour vertical transport, especially within the troposphere, plays a key role in the atmospheric water cycle. All water vapour in the atmosphere originates from surface evaporation and is first confined in the atmospheric boundary layer (ABL, Boutle et al., 2010), which is defined as the lowest layer of the atmosphere influenced by the Earth's surface (Stull, 1988). The water vapour is turbulently mixed in the ABL, making it act as a reservoir. Actually, all water vapour entering and transporting meridionally and zonally in the free troposphere (FT) is initially exported through the ABL (Bailey et al., 2013). In other words, the water vapour exchange between the ABL and the FT is a prerequisite for its large-scale transport and redistribution, as well as interaction with other constituents, in the upper atmosphere. Several studies indicate the importance of this key process on precipitation (Liu et al., 2020), cloud systems (Miura et al., 2007), tropical cyclone formation (Fritz and Wang, 2013), Madden–Julian oscillation (Hirota et al., 2018), West African Monsoon Jump (Hagos and Cook, 2007), and O_3 vertical distributions (Andrey et al., 2014). Therefore, it is of great significance to quantify the vertical exchange of water vapour between the ABL and FT.

However, the exchange between the ABL and FT is not straightforward, both for water vapour and air mass. Although the diurnal variation of the ABL depth allows air constituents

60 to be entrained into and left out of this layer within its variation range, the actual exchange
61 between ABL and FT is small on the time scale of more than one day due to the cancelling
62 effect (Hov and Flatoy, 1997; Jin et al., 2021). The current studies on water vapour vertical
63 transport are mainly limited to complex terrain areas or special convective events. The
64 local/mesoscale circulation induced by orographic thermal and dynamic effects is considered
65 a key process for ABL ventilation (Kossmann et al., 1999; McKendry and Lundgren, 2000;
66 Dacre et al., 2007). Henne et al. (2005) found that there were elevated moisture layers in the
67 lower free troposphere in the lee of the Alps resulting from mountain venting. On average for
68 the 12-year period, ~30% of the water vapour of the Alpine boundary layer was vented to the
69 FT per hour during the daytime, which makes the total precipitable water within the elevated
70 moisture layer increase by ~1.3 mm. Another simulated study indicates that the moisture
71 exchange between the ABL and FT of mountainous topography can be about 3–4 times larger
72 than the amount of moisture evaporated from the surface in a specific ventilation event (Weigel
73 et al., 2007). The convective system, mainly mesoscale deep and shallow convection, is another
74 important factor leading to the vertical transport of water vapour. The isotope observations
75 show that the moisture transport pathways to the subtropical North Atlantic FT are linked to
76 dry convection processes over the African continent which effectively injects humidity from
77 the ABL to higher altitudes (Gonzalez et al., 2016; Dahinden et al., 2021). The water vapour
78 budget of the free troposphere of the maritime tropics shows that 20% of this source comes
79 from vertical convective transport (Sherwood, 1996). On the other hand, an idealized
80 simulation suggests that the warm conveyor belt ascent and shallow convective processes
81 contributed about equally to FT moisture (Boutle et al., 2010, 2011).

82   Though for these studies, general characteristics of long-term and wide-ranging ABL-FT
83 water vapour exchange are still unknown. These characteristics are closely bound up with the
84 atmospheric energy flow and the entire climate system, affecting clouds, precipitation and
85 radiation (Sodemann and Stohl, 2013; Wong et al., 2018; Wypych et al., 2018). For example,
86 small variations in upper atmospheric humidity over a large space-time scale can cause
87 systemic changes in the hydrological cycle and atmospheric circulation (Minschwaner and
88 Dessler, 2004; Sherwood et al., 2010; Allan, 2012). The climate state of water vapour vertical
89 exchange flux is critical for quantifying these specific effects. To fill this knowledge gap, the
90 present study calculates the water vapour exchange flux between the ABL and FT for 7 years
91 (2011&2014-2019) over eastern China (20-42°N, 108-122°E) to establish the first quantitative
92 climatology view on this issue. The water vapour budget method is used, with the mesoscale
93 meteorological simulation providing input data. January, April, July, and October, respectively
94 representing winter, spring, summer, and autumn, are considered to discuss the seasonal
95 characteristics. Interannual differences are analysed by investigating the impact of El Niño and
96 La Ninã events. On the basis of understanding the foundational features, we further attempt to
97 discuss the role of ABL-FT water vapour exchange playing in anomalous precipitation. The
98 arrangement of this paper is as follows. Data and methods are described in Section 2. The
99 seasonal characteristics and mechanism analysis, interannual variability and the relation with

100   anomalous precipitation are presented and discussed in Section 3. Finally, the findings of this
101   study are summarized in Section 4.

102   **2 Data and methods**

103   **2.1 Observation data**

104   Intensive ABL sounding data and routine surface meteorological data were used to
105   evaluate the performance of the Weather Research Forecast (WRF) model that provided the
106   input data for estimating exchange flux.
107   Intensive ABL sounding data: Two field experiments of intensive GPS (Global
108   Positioning System) sounding were carried out in Dezhou (37°16′ N, 116°43′ E), located in the
109   middle of the North China Plain (NCP) (Fig. 1b), from December 25, 2017, to January 24,
110   2018, and from May 14 to June 14, 2018. Eight soundings were taken for each day, at 02:00,
111   05:00, 08:00, 11:00, 14:00, 17:00, 20:00 and 23:00 LT (i.e., UTC + 8). GPS radiosonde
112   (Beijing Changzhi Sci and Tech Co. Ltd., China) was used to obtain profiles of wind,
113   temperature and humidity with the ascending velocity being about 3-5 m s^{-1}. We eliminated
114   the outliers from the original data and averaged the profiles to an effective vertical resolution
115   of 10 m. ABL heights were determined with these data via the potential temperature profile
116   method (Liu and Liang, 2010). The reliability of the GPS sounding data has been systematically
117   evaluated by Li et al. (2020) and Jin et al. (2020).
118   Routine surface meteorological data: The hourly surface data of 137 routine observatories
119   distributed within the research domain were collected from the Chinese National
120   Meteorological Center. The dataset included information on wind speed and direction, air
121   temperature, relative humidity, air pressure, cloud coverage and precipitation, which was used
122   to evaluate the WRF simulation.

123   **2.2 Three-dimensional meteorological simulation**

124   The WRF model was conducted to provide three-dimensional meteorological data for the
125   estimation of ABL-FT water vapour exchange flux. Two nested domains (Fig. 1a) were
126   employed with horizontal grid lengths of 30 and 10 km, respectively. The inner covered eastern
127   China (20–42°N, 108–122°E), the main research region for the ABL-FT water vapour
128   exchange in the present work (Fig. 1b). Each domain had 37 vertical layers extending from the
129   surface to 100 hPa, with the vertical resolution being about 20-30 m below 200 m, increasing
130   to ~100 m at 750 m, ~250 m at 2000 m, ~350 m at 3000 m, ~600 m at 5000 m, ~900 m at 8000
131   m, ~1300 m at 11000 m and gradually enlarging to the top of the model. There were 24 layers
132   within 3 km to resolve the ABL and its upper FT. The meteorological initial and boundary
133   conditions were set using the US National Center for Environmental Prediction Final Analysis
134   (NCEP-FNL) dataset.
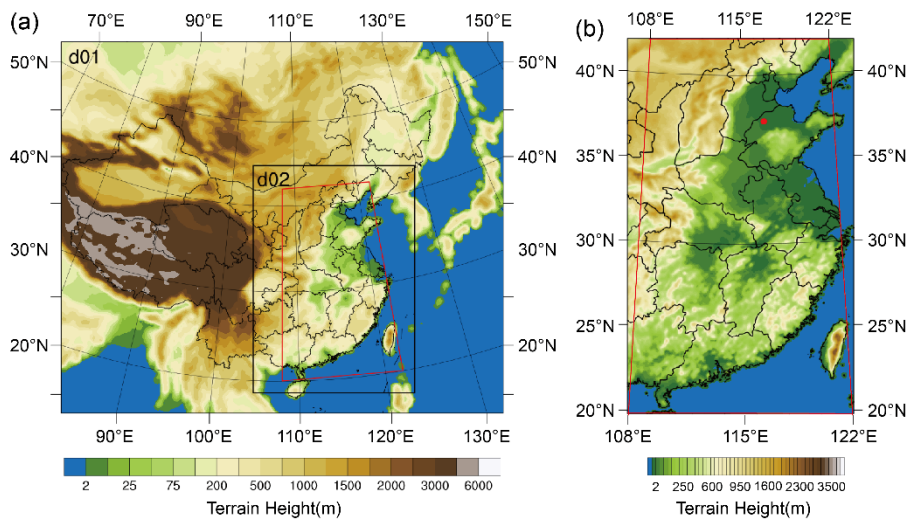
Figure 1. Geographical map of (a) the Weather Research and Forecast (WRF) model domains (d01 and d02) and (b) the amplified research domain (marked with red lines). The map uses the Lambert projection with the centre meridians of 108°E in (a) and 115°E in (b). The red dot in (b) indicates the intensive GPS sounding observatory.

In order to adequately reproduce water vapour distribution and to correctly estimate the ABL-FT exchange flux, sensitivity simulations were carried out to choose reasonable physical parameterization schemes. We focused on the microphysical and cumulus parameterizations that are the most relevant to the moisture simulation. Microphysics in the model includes explicitly resolved water vapour, cloud and precipitation processes. Cumulus schemes are responsible for the sub-grid scale effects of convection and/or shallow clouds. Vertical fluxes due to unresolved updrafts and downdrafts are represented. Lin et al. scheme (Lin et al., 1983) and WRF Single-Moment 6-class (WSM6) scheme (Hong and Lim, 2006) in microphysics parameterization, and Grell-Devenyi (GD) ensemble scheme (Grell and Devenyi, 2002) and Kain-Fritsch (KF) scheme (Kain, 2004) in cumulus parameterization were compared, which were most commonly used in previous moisture simulation studies (Perez et al., 2010; Gonzalez et al., 2013; Jain and Kar, 2017; Qian et al., 2020). Other physics parameterization schemes used in this study included the Yonsei University PBL scheme (Hong et al., 2006), the Noah land surface Model (Chen and Dudhia, 2001), the Dudhia shortwave radiation scheme (Dudhia, 1989), and the rapid radiative transfer model (Mlawer et al., 1997) for longwave radiation. WRF simulations were initialized at 00 UTC on the day and there was a 12-h spin-up time before the start of each 48-h simulation. Domain outputs were sampled every hour for the whole simulation period (January, April, July, and October in 2011 and 2014-2019).

These schemes were evaluated by comparing simulated and observed specific humidity, temperature and wind speed, from their near-surface temporal evolution and vertical spatial structure. Another two key parameters, ABL height and precipitation were also concerned: the former directly affects the exchange flux results, and the latter characterizes the moisture budget. The hourly averages of model outputs were extracted from the grid points nearest to the observed sites for comparison. In the vertical direction, the modelled and sounding data

were simultaneously interpolated into the same height with 10 m intervals ranging from 50 m to 3 km. Note that the ABL height was diagnosed with the potential temperature profile method both for the simulations and for observation data, rather than using the default bulk Richardson number method in the YSU scheme.

The results of sensitivity experiments showed that there were no appreciable differences among various microphysical and cumulus parameterization schemes (Table S1 and S2). In comparison, the combination of the WSM6 scheme and GD scheme performed better in humidity simulation and was more effective in reproducing temperature, wind speed and ABL height, especially in summer (Table S2). Therefore, these schemes were used in the present study. Its simulation performance determines the reliability of the calculated flux results and thus a comprehensive evaluation is provided here. The spatial-temporal evolutions of modelled and observed meteorological fields are presented by the height-time cross sections of specific
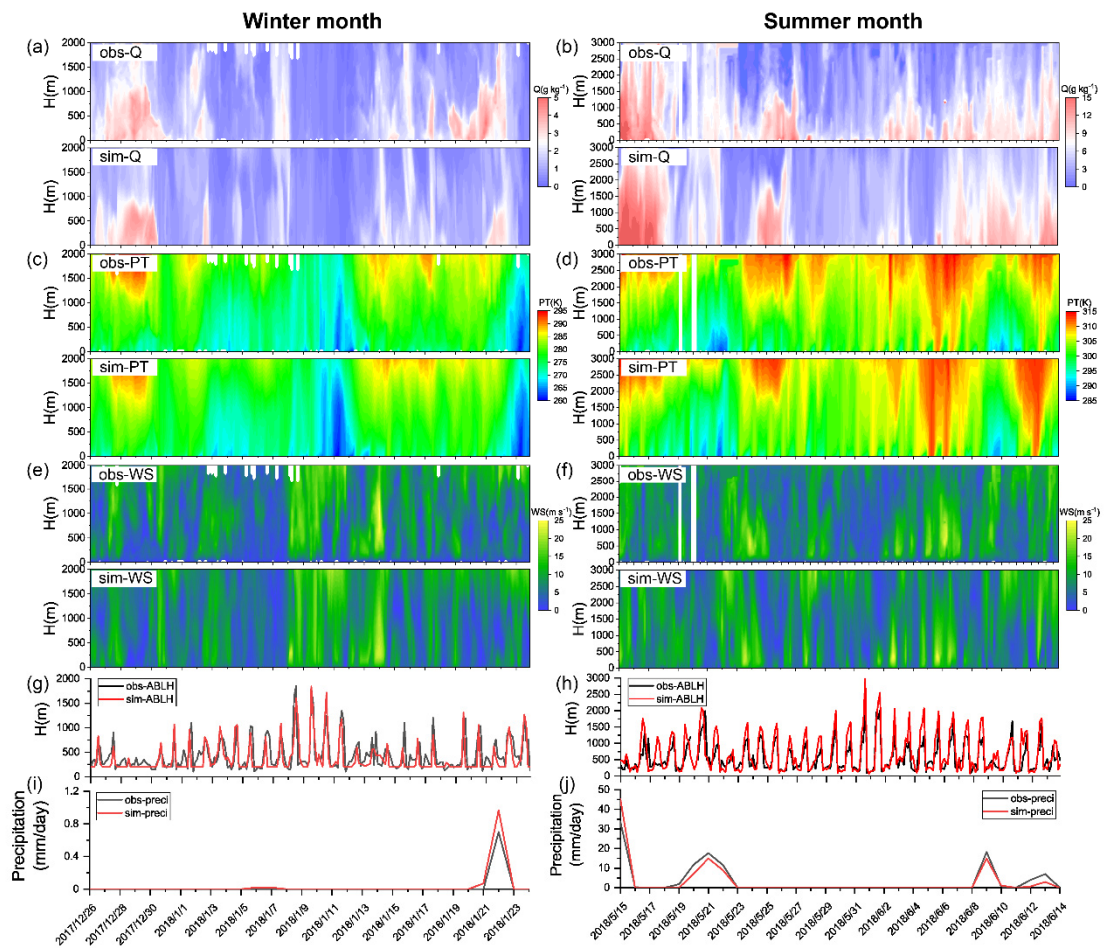
Figure 2. Observed and simulated time-height cross-sections of (a-b) specific humidity, (c-d) potential temperature, (e-f) wind speed, and temporal evolution of (g-h) ABL height and (i-j) daily cumulative precipitation at the Dezhou site (37.27°N, 116.72°E) during winter (from December 26, 2017, to January 24, 2018) and summer (from May 15, 2018, to June 14, 2018) months of intensive GPS sounding field experiment. The time resolution of sounding data in (a-h) is 3-hr. The Y-axis scales are different in the winter panel and the summer panel.

humidity, potential temperature and wind speed, as well as the ABL height and precipitation (Fig. 2). During the winter and summer months of the intensive GPS sounding, the simulated atmospheric thermal and dynamic structures were comparable with observations. The alternating between dry and wet atmospheric states (Fig. 2a-b), formation and decay of upper temperature inversion (Fig. 2c-d), and vertical location and temporal transition of the strong and weak wind layers (Fig. 2e-f) were successfully reproduced. Accordingly, a good correlation between the simulated and observed ABL height was achieved, both in terms of diurnal variation and synoptic evolution lasting several days (Fig. 2g-h). The correlation coefficients were 0.71 and 0.84 during wintertime and summertime, respectively. It should be mentioned that there was a slight discrepancy in the modelled ABL heights (mean biases are about -70 m and 120 m in winter and summer), which may further affect the identification of other parameters (such as the wind component) at the ABL top and lead to uncertainty in the calculation results. This impact will be quantitatively analysed in the discussion section. Another concerned meteorological factor, the daily cumulative precipitation was also evaluated, which showed a consistent evolution in observation and simulation (Fig. 2i-j) with correlation coefficients as high as 0.99 and 0.91 (p<0.05) in winter and summer respectively, demonstrating that the moisture budget is accurately captured by the WRF simulations. Overall, the model showed the ability to capture the major variation of observed atmospheric thermal-dynamical structures reasonably, which ensures the validity of the meteorological inputs for the ABL-FT exchange flux calculation.

2.3 ABL-FT water vapour exchange flux

Similar to mass vertical exchange (Sinclair et al. 2010; Jin et al., 2021), the estimation of ABL-FT water vapour exchange flux in this study was based on an ABL water vapour budget equation established by Boutle et al. (2010):

$$\frac{\partial}{\partial t}\left(\int_0^h \rho q\, dz\right) = -\left(\frac{\partial}{\partial x}\int_0^h \rho q u\, dz + \frac{\partial}{\partial y}\int_0^h \rho q v\, dz\right) + (\rho q)_h\left(\frac{\partial h}{\partial t}\right)$$

$$-(\rho q)_h\big(\vec{U}\cdot\vec{n}\big)_h - \big(\rho\overline{w'q'}\big)_h + \big(\rho\overline{w'q'}\big)_0 + P, \qquad (1)$$

where ρ is air density, q is water vapour mixing ratio, h is the ABL height, $\vec{U} = (u, v, w)$ is wind vector, $\vec{n} = (-\frac{\partial h}{\partial x}, -\frac{\partial h}{\partial y}, 1)$ is the unit normal vector perpendicular to the ABL top surface, w' and q' are the fluctuation values of vertical velocity and water vapour content respectively. P is the precipitation. Subscripts h and 0 indicate quantities at the ABL top and the surface. The first term on the right side of Eq. (1) represents horizontal convergence/divergence within the ABL, the second term indicates the local change in ABL depth, the third term indicates vertical advection across the ABL top, the fourth and fifth terms are turbulent transport at the ABL top and the surface respectively, and the last term indicates the net precipitation falling through the ABL.

Denoting the water vapour vertical exchange flux between the ABL and FT as F (positive values represent upward transport), it can be further written as:

$$220 \qquad F = -\left((\rho q)_h \left(\frac{\partial h}{\partial t}\right) - (\rho q)_h (\vec{U} \cdot \vec{n})_h - \left(\rho \overline{w'q'}\right)_h\right)$$

$$221 \qquad \approx -\left((\rho q)_h \frac{\partial h}{\partial t} + (\rho q)_h \left(u_h \frac{\partial h}{\partial x} + v_h \frac{\partial h}{\partial y}\right) - (\rho q)_h w_h\right). \qquad (2)$$

222 Since turbulent transport between the ABL and FT is typically related with dryer air that does
223 not affect the total moisture content, $\left(\overline{w'q'}\right)_h$ is usually considered to be a negligible
224 contribution to the ABL-FT water vapour exchange flux (Boutle et al., 2010). Specifically, the
225 finite difference method was adopted for calculation with the time step being 1 hr, and the
226 horizontal dimensions of the model grid being 10 km. The ABL heights were obtained from
227 the hourly output of the WRF model. Other variables at the ABL top were extracted from the
228 nearest model level above the ABL height (there is no significant difference between these
229 extracted values and those interpolated to the ABL top). It is clear that the water vapour vertical
230 exchange flux between the ABL and FT is determined by i) the local temporal variation of
231 ABL height, $\frac{\partial h}{\partial t}$, allowing the water vapour entrained into the ABL or left in the upper
232 atmosphere; ii) the spatial variation of the ABL, making water vapour horizontally advected
233 across an inclined ABL top; and iii) the vertical advection motion, carrying water vapour
234 downward/upward through the interface between the ABL and FT. These three flux
235 components are denoted as F_{local}, F_{hadv}, and F_{vadv}, and their contributions and evolutions will
236 be discussed in the following.

237 **3 Results and discussion**

238   The present study is based on a 7-year flux calculation. The years 2011&2014-2019 are
239 selected for analysis, which includes typical La Niña, El Niño, and neutral years (Marchukova
240 et al., 2020; You et al., 2021; Felix Correia Filho et al., 2021), and are considered to be valid
241 and concise datasets to reflect the characteristics of water vapour exchange between the ABL
242 and FT. Their climatic representativeness is demonstrated using a long-term historical dataset
243 provided by the fifth generation ECMWF (European Centre for Medium Range Weather
244 Forecasts) reanalysis (Hersbach et al., 2023, download from the website
245 https://cds.climate.copernicus.eu/cdsapp#!/dataset/reanalysis-era5-pressure-levels?tab=form).
246 We compare the features of key meteorological elements during the study period (2011&2014-
247 2019) and over the past 30 years (1990-2019) by the Kolmogorov-Smirnov test (K-S test) and
248 histogram analysis. Temperature, three-dimensional wind component, specific humidity both
249 near the surface and at the upper level, as well as the ABL height and precipitation, are
250 concerned. The K-S test indicates that there is no significant difference (with a confidence level
251 of 95%) between the 7-year sample period and the 30-year historical dataset for these variables
252 (Table S3). The histogram analysis further illustrates that their normalized frequencies in the
253 research samples are similar to those in the long-term historical data (Fig. S1). Also, the annual
254 variation of the two sets of data presents a high consistency, with similar mean values and
255 standard deviations (Fig. S2). The above analysis verifies that the 7-year samples adopted in

256 this study can represent the long-term climatology, and be promising to obtain climatic features
257 of water vapour exchange between the ABL and FT. The basic temporal and spatial patterns,
258 influencing mechanism, and relationship with ENSO and extreme precipitation are revealed as
259 follows.

3.1 Seasonal generality and variability

3.1.1 Spatial distribution

262 Figure 3 shows the spatial distribution of water vapour exchange flux between the ABL
263 and FT in the research domain (20-42°N, 108-122°E, marked by red lines in Fig.1), averaged
264 over all 7-year (2011, 2014-2019) for January, April, July, and October. It is obvious that the
265 ABL-FT water vapour exchange in the south and north of the research domain is different,
266 because they are affected by subtropical and temperate climates, respectively (Domroes and
267 Peng, 1988; Zheng et al. 2013; Zhang et al., 2020). Therefore, the southern (20-32°N, 108-
268 122°E) and northern (32-42°N, 108-122°E) regions are divided for analysis (the boundary is
269 marked in Fig. 3). The water vapour exchange is more active in the southern region with more
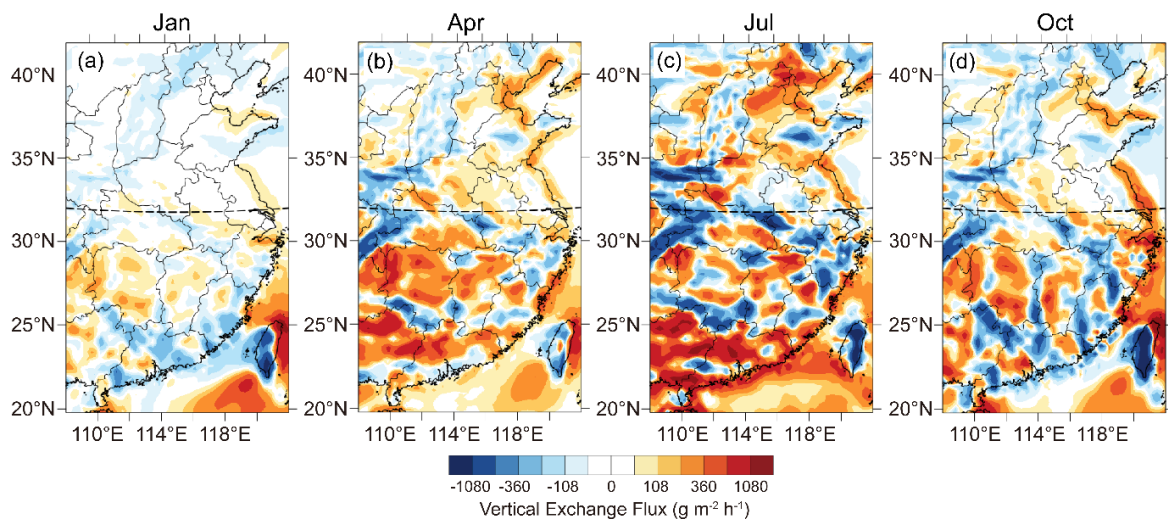
Figure 3. Spatial distribution of ABL-FT water vapour exchange fluxes in eastern China, averaged over 7 years for (a) January, (b) April, (c) July, and (d) October. Black dashed lines mark the boundary between the northern (32-42°N, 108-122°E) and southern (20-32°N, 108-122°E) regions. Positive and negative fluxes (warm and cool colours) represent water vapour upward and downward transport at the ABL and FT interface.

276 pronounced spatial variability, and tends to output from the ABL. In the northern region,
277 vertical exchange fluxes and spatial differences are relatively small. From another perspective,
278 the vertical exchange of water vapour is closely related to the topographic distribution (Fig.
279 1b), which is manifested as strong exchange activities usually occurring around mountainous
280 or coastal areas, both in the northern and southern regions. This feature is similar to the spatial
281 pattern of the air mass exchange flux between the ABL and the FT indicated by Jin et al. (2021).
282 It is the result of the dynamical interaction of topography on the synoptic system, and thermal

283 property difference over the heterogeneous underlying surface (Kossmann et al., 1999; Dacre
284 et al., 2007; Jin et al., 2021). These phenomena will be detailedly explained in the mechanism
285 analysis in Sect. 3.2.

3.1.2 Seasonal difference

287 Corresponding to Fig. 3, the spatial means of ABL-FT water vapour exchange flux and
288 their seasonal evolutions for northern and southern regions are shown in Fig. 4. They are
289 obtained by grid averaging in the ranges of 32-42°N, 108-122°E and 20-32°N, 108-122°E,
290 respectively. Obviously, the exchange flux varies from season to season in both regions. For
291 the northern region, winter and autumn (represented by January and October, respectively) are
292 characterized by water vapour transport downward from the FT into the ABL, with the spatial
293 mean fluxes of -15.6 and -18.8 g m^{-2} h^{-1} (1 g m^{-2} h^{-1} =10^{-3} mm h^{-1}) and the standard deviation
294 of 3.6 and 8.6 g m^{-2} h^{-1} over 7 years. While in spring and summer (represented by April and
295 July, respectively), the northern region as a whole presents an upward export of water vapour
296 from the ABL to the FT, with the regional mean fluxes being 6.4 and 11.9 g m^{-2} h^{-1}. They are
297 characterized by more significant inter-annual variations than the exchange fluxes in the cold
298 seasons. In the southern region, the water vapour vertical exchange is featured with ABL output
299 in all seasons, with a winter minimum and a summer maximum. The mean upward fluxes vary
300 greatly, showing one order of magnitude greater in April and July (99.1 and 115.51 g m^{-2} h^{-1})
301 than in January and October (9.6 and 16.7 g m^{-2} h^{-1}), accompanied by the larger standard
302 deviation (50.4 and 68.4 g m^{-2} h^{-1}). The notable interannual variability in the warm season may
303 be related to the ENSO phenomenon, which will be discussed in the following section.
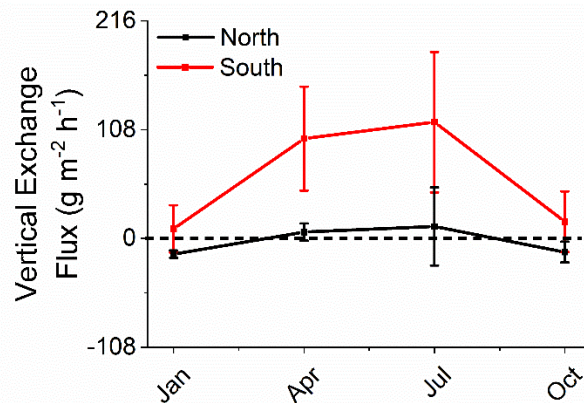
304

305 Figure 4. Seasonal variation of average ABL-FT water vapour exchange fluxes and their standard
306 deviations over the northern region (32-42°N, 108-122°E) and southern region (20-32°N, 108-122°E)
307 during 7 years. Positive and negative fluxes represent water vapour upward and downward transport
308 between the ABL and FT.

309 In order to better understand the magnitude of water vapour exchange between the ABL
310 and FT, we compare the transport flux with the surface evaporation rate (Table 1). It indicates
311 the "emission intensity" of water vapour from the surface, which varies in different regions and
312 seasons. The surface evaporation rates in the northern and southern regions have maximums in

313 summer (122.4 g m^{-2} h^{-1} and 194.4 g m^{-2} h^{-1}) and minimums in winter (21.6 g m^{-2} h^{-1} and 108.0

314 g m^{-2} h^{-1}). Obviously, the evaporation in the north is weaker than that in the south, especially

315 in winter, it is only one-fifth of that in summer. Consequently, for the northern region, during

316 the cold seasons with the dry land surface, the ABL-FT water vapour exchange is downward

317 and the input flux is 37%-72% of the surface evaporation rate. Although the specific humidity

318 decreases with height, counter-gradient transport still occurs reasonably because the ABL-FT

319 exchange is a typically non-local mixing process (Stull 1988; van Dop and Verver, 2001;

320 Ghannam et al., 2017). This suggests the ABL is a net moisture sink of upper layer FT air,

321 which plays a role in maintaining water vapour within this layer. As surface evaporation

322 intensifies in the warm months, water vapour is exported from the ABL in April and July, and

323 the upward flux accounts for 10% of the evaporation rate. In the southern region with relatively

324 strong evaporation, the ABL water vapour is always transported upward to the FT. The output

325 flux is about 10% of the evaporation rate in January and October, and this ratio is as high as

326 60%-80% in April and July, indicating that the ABL acts as an effective water vapour source

327 to the upper atmosphere.

328 Table1. Comparison of ABL-FT water vapour exchange flux (g m^{-2} h^{-1}, positive for upward, negative

329 for downward) and surface evaporation rate (g m^{-2} h^{-1}, positive for upward) in the northern and southern

330 regions.

Region	Process	Jan	Apr	Jul	Oct
North	ABL-FT exchange	−15.6	6.4	11.9	−18.8
	Surface evaporation	21.6	61.2	122.4	50.4
South	ABL-FT exchange	9.6	99.1	115.5	16.7
	Surface evaporation	108.0	115.2	194.4	144.0

3.2 Main influential mechanism

332 As shown in Eq. (2), three physical terms contribute to the total ABL-FT exchange, i.e.,

333 the local temporal variation of ABL height (F_{local}), the horizontal advection across the spatial

334 inclined ABL top (F_{hadv}), and the vertical motion through the ABL-FT interface (F_{vadv}). It is

335 of interest to clarify the specific effects of these factors on water vapour vertical exchange and

336 their seasonal characteristics. Results of the monthly mean and diurnal cycle over the 7 years

337 are presented below respectively.

338 The monthly mean results show that the term F_{vadv} is the most significant to total ABL-

339 FT moisture exchange flux (Fig. 5, green bar). In the northern region, this term produces

340 persistent downward flux (−19.5~−44.7 g m^{-2} h^{-1}, Fig. 5a), which substantially offsets the

341 upward flux caused by the other two terms, so that the ABL water vapour presents net input

342 during cold months (i.e., January and October) and weak output in warm seasons (i.e., April

343 and July). For the southern region, it induces small downward fluxes in January and October

344 (−18.6 and −5.5 g m^{-2} h^{-1}) while large upward flux in April and July (60.7 and 68.6 g m^{-2} h^{-1}),

345 which results in the total water vapour exchange as weak and strong output from the ABL
346 during cold and warm months, respectively (Fig. 5b).
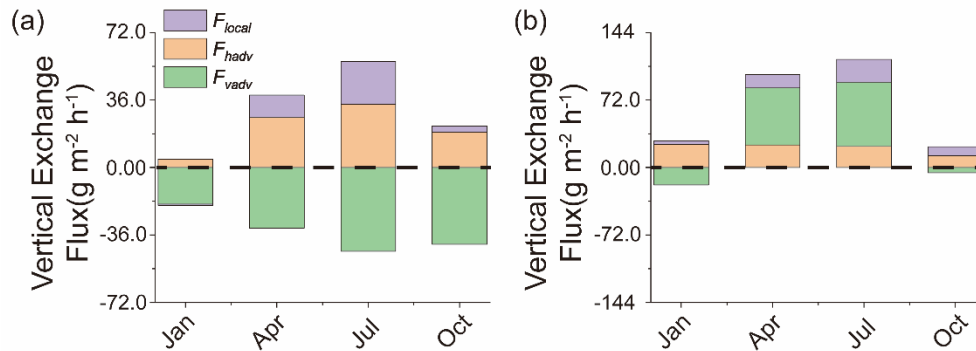
348 Figure 5. Contributions of three components (F_{local}, F_{hadv}, and F_{vadv}) to the total ABL-FT water
349 vapour exchange flux. Results are spatial mean over the (a) northern (32-42°N, 108-122°E) and (b)
350 southern (20-32°N, 108-122°E) regions of eastern China respectively. F_{local}: local temporal variation
351 of ABL height (purple bar); F_{hadv}: advection across the spatial inclined ABL top (yellow bar); F_{vadv}:
352 vertical motion through the ABL-FT interface (green bar). Positive and negative fluxes represent water
353 vapour upward and downward transport between the ABL and FT. The Y-axis scales are different in
354 (a) northern and (b) southern regions.

355   The upward/downward transport of water vapour caused by the term F_{vadv} depends on
356 the direction of the vertical motion. The spatial distributions of the vertical velocity are
357 presented in Fig. 6, accompanied by horizontal wind fields at the ABL top, as well as terrain
358 heights. The upward motions usually occur on the windward of the mountains, while the
359 descending velocities appear on the leeward side, in each season. This is attributed to the
360 dynamic forcing of the terrain on seasonal mean winds. Due to the alternation of winter and
361 summer monsoons throughout the year, the vertical motion pattern varies accordingly in four
362 representative months (Fig. 6a-d). In the winter, the Siberian high invades from the northwest
363 and forms strong northerly winds (Fig. 6e). In the northern region, the prevailing northwest
364 airflows overcome the obstruction of Taihang Mountain and intensely descend on its leeward
365 side (Fig. 6a). As the air migrates south, the dominant airflow deflects northeasterly (Fig. 6e),
366 and the vertical motion manifests more upward velocities in front of the major mountainous
367 region, and more downward velocities behind these mountains (Fig. 6a). During the summer,
368 southerly air flows dominate eastern China and gradually weaken from south to north (Fig. 6g).
369 The southern region is characterized by obvious forced uplift on the windward side of the major
370 mountains (Fig. 6c). The onshore airflow convergence of the prevailing southerly winds in
371 coastal areas also produces upward motions (Fig. 6c). These factors are conducive to the
372 vertical output of ABL water vapour in the southern region during warm months. The northern
373 region is less invaded by the summer monsoon: only the eastern part of the NCP is affected by
374 southerly winds to induce upward motion in the piedmont, while the western part is still
375 dominated by westerly winds leading to systematic subsidence (Fig. 6c, g). The general
376 patterns of vertical velocity fields provide an explanation for the water vapour exchange fluxes
377 caused by the term F_{vadv}. It is noticed that, although the ABL-FT water vapour exchange fluxes

in Fig. 3 are averages over 7 years, there still exists obvious spatial heterogeneity. Smooth variations in both the mean wind field (Fig. 6e-h) and mean ABL height (Fig.S5) indicate these two factors are not related to the flux heterogeneity. But there indeed exists discontinuous structures in the vertical velocity fields at the ABL top (Fig.6a-d), which is significant to water vapour exchange flux. There can be smaller-scale secondary vertical motion being stimulated when prevailing airflows encounter diverse terrains (Fig. S4). Multiscale dynamical interactions between complex terrain and synoptic processes should be of great significance to the water vapour exchange between the ABL and FT.
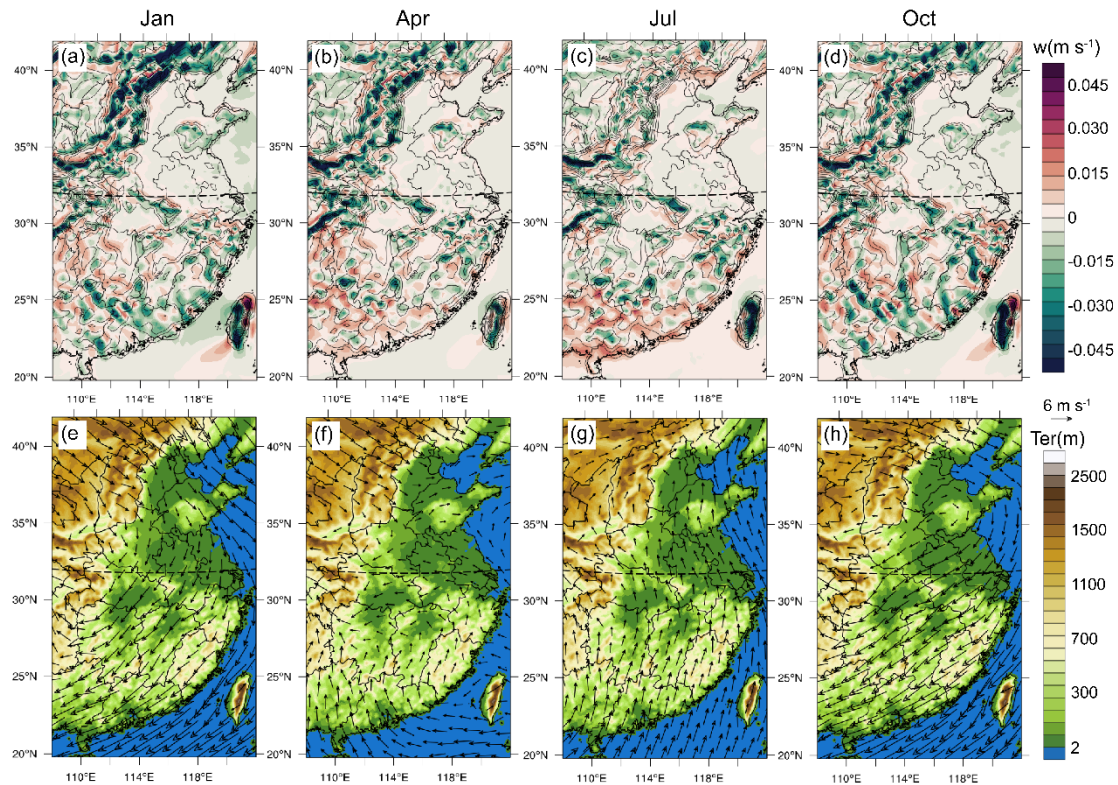
Figure 6. Spatial distribution of (a-d) vertical velocities at the ABL top and (e-h) terrain height superposed with horizontal wind vectors averaged over 7 years for January, April, July, and October. Positive values represent upward motions and the contours in (a-d) represent the terrain height. Black dashed lines mark the boundary between the northern (32-42°N, 108-122°E) and southern (20-32°N, 108-122°E) regions.

The horizontal advection term F_{hadv} tends to allow water vapour to be out of the ABL and the magnitude increases in spring and summer (Fig. 5, yellow bar). This water vapour exchange component mainly occurs in the mountain-plain transition zone and the land-ocean boundary (Fig. S3e-h), where the ABL is unevenly distributed due to the heterogeneous surface properties (Fig. S5). During the warm season, the thermal difference is more obvious with the solar radiation strengthening and thereby with larger spatial variation of the ABL, especially in the northern region. This explains the seasonal variation of the water vapour exchange flux caused by the term F_{hadv}.

400   The temporal ABL height variation term F_{local} contributes relatively less to the total water
401   vapour exchange (Fig. 5, purple bar). Noticeably, this average flux component is positive,
402   being negligible in autumn and winter (0.7~3.3 g m^{-2} h^{-1}), but becoming relatively pronounced
403   in spring and summer (12.0~24.5 g m^{-2} h^{-1}). This is inconsistent with the air mass exchange
404   between the ABL and FT, in which the monthly average flux caused by this term is always
405   insignificant because the ABL entrainment and detrainment of the air mass cancel out each
406   other in a diurnal cycle (Jin et al., 2021). To understand more details of the term F_{local} in the
407   ABL-FT water vapour exchange, the mean diurnal variation of the exchange flux is derived
408   and shown in Fig. 7.
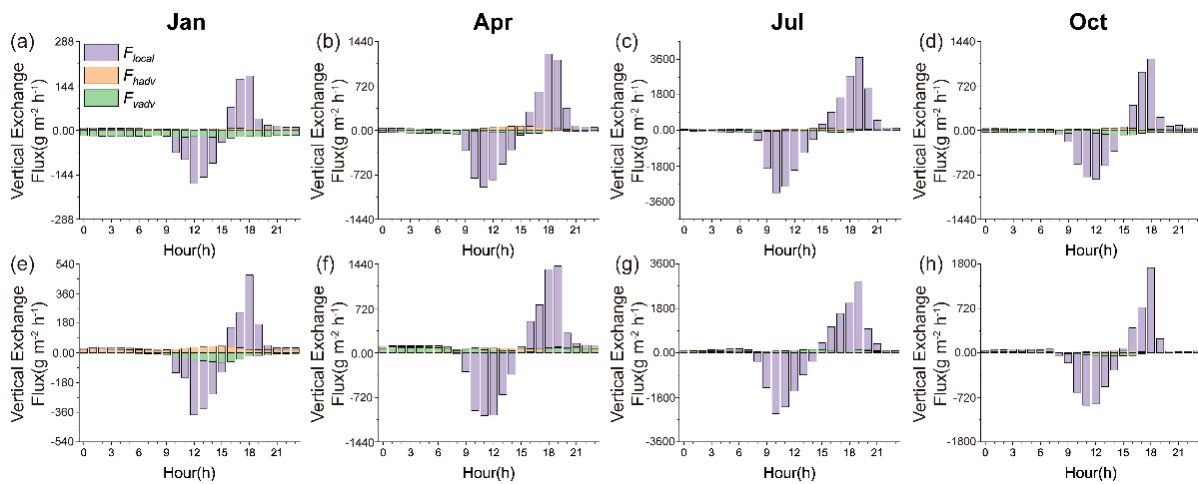
409

410   Figure 7. Diurnal variation of the three exchange flux components (F_{local}, F_{hadv}, and F_{vadv}) over the
411   (a-d) northern region (32-42°N, 108-122°E) and (e-f) southern region (20-32°N, 108-122°E) averaged
412   for (a, e) January, (b, f) April, (c, g) July, and (d, h) October. F_{local}: local temporal variation of ABL
413   height (purple bar); F_{hadv}: advection across the spatial inclined ABL top (yellow bar); F_{vadv}: vertical
414   motion through the ABL-FT interface (green bar). Positive and negative fluxes represent water vapour
415   upward and negative downward transport between the ABL and FT. The Y-axis scales are different in different
416   months and different regions.

417   At a first sight of the daily cycle, F_{local} is the absolutely dominant term in all seasons and
418   both northern and southern regions (Fig. 7, purple bar), corresponding to the diurnal variation
419   of the ABL height (shown in Fig. S6). When the unstable ABL develops in the morning, the
420   water vapour in the residual layer is entrained into the ABL; while as the daytime ABL
421   collapses in the later afternoon, a large part of water vapour is left aloft the newly formed stable
422   ABL. Note that, unlike the air mass exchange at the ABL top, the water vapour entrained
423   (input) flux is less than the output flux, especially in spring and summer. This difference can
424   be attributed to the fact that the surface is, in general, a continuous evaporation source
425   throughout a diurnal cycle. Turbulent mixing brings water vapour upward in the ABL depth,
426   and forms a net upward flux across the ABL top. This is also the reason why a larger magnitude
427   of F_{local} exists in the warm seasons when there is stronger surface evaporation. Although the
428   ABL temporal variation term F_{local} dominates the diurnal variation of the total ABL-FT

moisture exchange flux, it contributes only a weak net output of water vapour in a monthly average flux, in comparison with the vertical motion term F_{vadv}, as mentioned above.

3.3 Interannual variability and its relation with ENSO

A climatic mean of the ABL-FT water vapour exchange over eastern China is presented above. Critically linked to the atmospheric water cycle, the exchange flux and its interannual variation are of great interest. It is well known that the atmospheric water cycle is significantly affected by El Niño and southern oscillation (ENSO), which is a joint phenomenon of the ocean and the atmosphere appearing as a recurring anomaly of the sea surface temperatures in the tropical Pacific and a seesaw of sea level pressure anomalies between Tahiti and Darwin. The El Niño (warm phase) and La Niña (cold phase) are the two extremes of ENSO (Walker and Bliss, 1932, 1937; Kousky et al., 1984; Wolter and Timlin, 2011). Considerable work has been conducted on the relationship between ENSO and wet and dry variability, water vapour horizontal transport, and precipitation events (Diaz, 2000; Knippertz and Wernli, 2010; Felix Correia Filho et al., 2021). However, little is known about the ABL-FT water vapour exchange during ENSO events. Here we take July as the research object, the month with the largest variability (shown in Fig. 4), to investigate the interannual difference of ABL-FT water vapour exchange fluxes affected by the ENSO phenomenon.
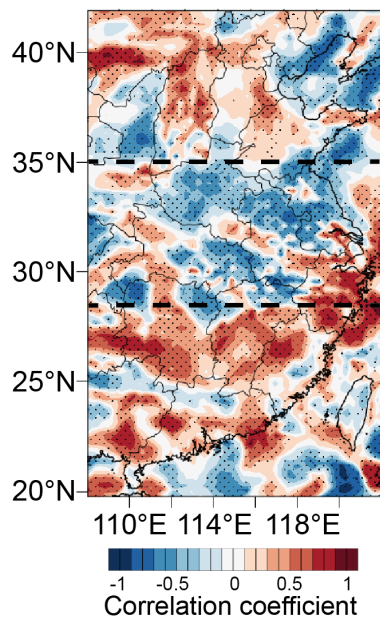
Figure 8. Spatial distribution of correlation coefficient between the water vapour exchange flux anomalies and Niño-3.4 index in July for 7 years. The dots indicate statistically significant grids and the black dashed lines indicate the triple distribution.

The correlation between the water vapour exchange flux anomalies and the Niño-3.4 index during the study period (2011&2014-2019) is quantitatively calculated. The former (anomaly or variability) is derived from the difference of each year with the 7-year average, and the latter is obtained from the website https://psl.noaa.gov/gcos_wgsp/Timeseries/Nino34/, representing

the average equatorial sea surface temperature across the Pacific from about the dateline to the South American coast (5°N-5°S, 170°W-120°W), which is the most commonly used indices to define El Niño and La Niña event. The statistical result shows that there is a significant correlation between the two factors, with about 65% of the grids meeting the 95% confidence level. A positive-negative-positive triple distribution is presented in the correlation map (Fig. 8). On this basis, the sensitive areas are identified, in which the water vapour exchange fluxes are further analysed. The central region (28-35°N, 108-122°E) has the most obvious significance, where the proportion of significant grids is as high as 70%. This area shows a negative correlation, i.e., the mean vertical output flux of water vapour is enhanced by about 57.6~151.2 g m^{-2} h^{-1} in cold phase La Niña years (2011 and 2016, blue boxes in Fig. 9a), and vice versa in warm phase El Niño years (2015 and 2019, red boxes in Fig. 9a), and the flux anomalies are close to 0 in neutral years (2014, 2017, and 2018, black boxes in Fig. 9a). In south (20-28°N, 108-122°E) and north (35-42°N, 108-122°E) areas with positive correlation coefficients, the trend is reversed. That is, the ABL moisture ventilation flux weakens 79.2~140.4 g m^{-2} h^{-1} in La Niña years and increases 108~194 g m^{-2} h^{-1} in El Niño years (figure not shown). This provides an explanation for the interannual variation of the water vapour exchange flux mentioned in Sect. 3.1.2.
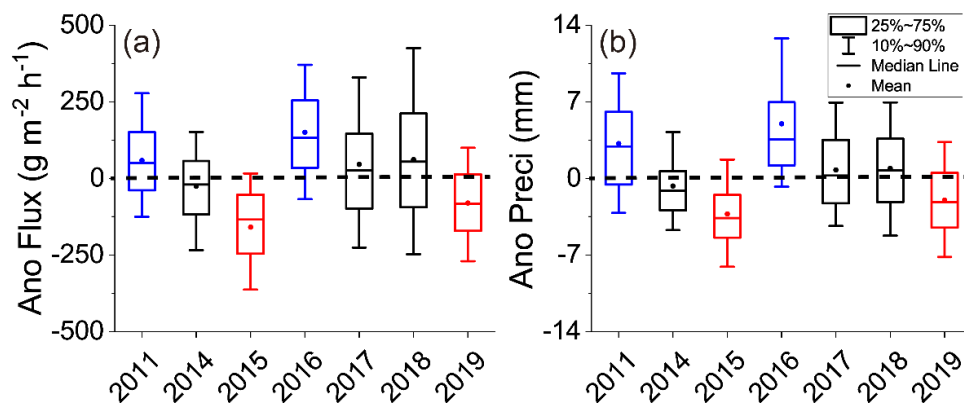
Figure 9. Anomalies of (a) water vapour exchange flux and (b) precipitation in July over the central region (28-35°N, 108-122°E, indicated in Fig. 8) during 2011&2014-2019. Blue, red and black indicate La Niña years, El Niño years and neutral years, respectively. Upper and lower sides of the box are the 75th and 25th percentile, and whiskers are the 90th and 10th percentile. Hollow squares and black lines in the box are mean and median.

In order to elucidate why the water vapour vertical exchange flux varies with ENSO, we further analyse three exchange components anomalies in El Niño and La Niña years (Fig. S7). Among them, the term F_{vadv} presents the most obvious correspondence with the correlation pattern (Fig.8), demonstrating that vertical motion and water vapour content at the ABL top are crucial influencing factors. We select the central region (with the most significant correlation) for detailed analysis. As shown in Fig.10, in La Niña year (represented by 2016), the upward vertical velocity strengthened and the water vapour mixing ratio increased in the central area, while the opposite trend was observed in El Niño year (represented by 2015). This

phenomenon is attributed to the stronger East Asian monsoon that brings more water vapour from the south and facilitates convergence to uplift during the cold phase period of ENSO, while in the warm phase, the weaker southerly wind reduces water vapour transport and is not conducive to convergence within the ABL (Zhou et al. 2012; Xue et al., 2015; Gao et al., 2018), which explains the increase or decrease of ABL water vapour output affected by ENSO.
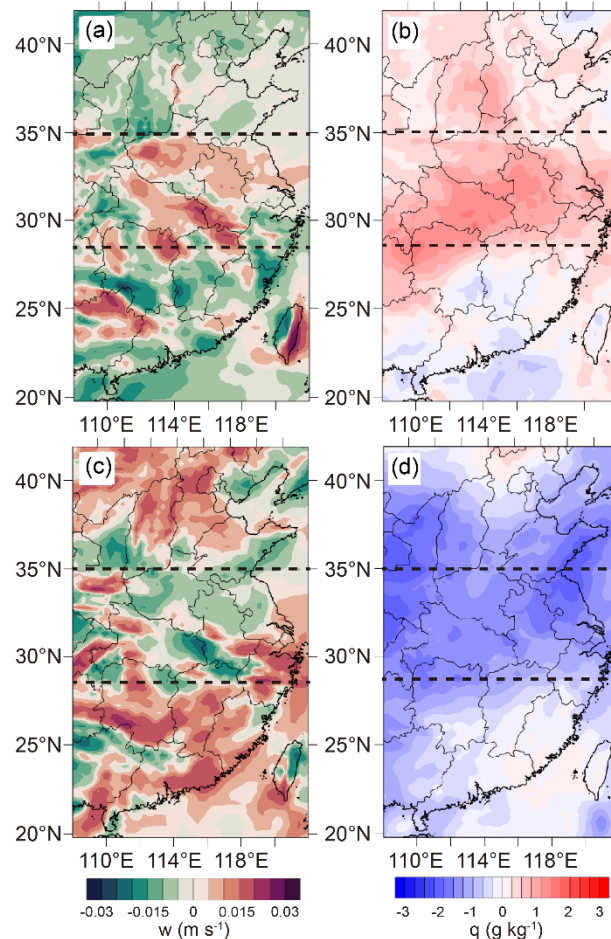
Figure 10. Spatial distribution of anomalies of vertical velocities (left) and water vapour mixing ratio (right) at the ABL top in July of (a-b) 2016 (La Niña year) and (c-d) 2015 (El Niño year).

Previous observation climatological studies have indicated that the summer precipitation anomalies in La Niña/ El Niño years are characterized by a tripolar distribution over eastern China (Wang et al., 2020), similar to water vapour exchange flux anomalies revealed in this work. It is of interest to investigate the relationship between water vapour vertical exchange and precipitation under the influence of ENSO. Taking the central region (28-35°N, 108-122°E) as an example, the precipitation anomalies present a good correspondence with the variations of the ABL-FT water vapour exchange flux (Fig. 9). Specifically, precipitation increases (decreases) about 3.2-6.9 mm (2.8-3.5 mm) when the vertical output of water vapour intensifies (weakens) in La Niña (El Niño) years. That is, enhanced water vapour output flux from the ABL to the FT tends to produce increased precipitation and vice versa. These results imply that, upper layer FT water vapour supplement from the ABL can also be a significant factor in changing regional precipitation, in addition to horizontal transport.

505   It should be stated that the above results are preliminary and rough, due to the limitations
506   of the sample. The response of the ABL-FT water vapour exchange to ENSO, and its impact
507   on precipitation, are complicated. The isolated patches in Fig. 8 and Fig. 10, as well as the box
508   and whisker in Fig. 9 (being 75th-25th and 90th-10th percentile of the flux/precipitation
509   anomalies), reflect the complex spatial variability over the research domain, which is not
510   thoroughly analysed in the current work. Nevertheless, this general result points to an
511   association among ABL-FT water vapour exchange, ENSO, and extreme precipitation, which
512   should be paid more attention to in future research.

513   **3.4 Discussion**

514   The present results are based on numerical simulations. Although reasonable
515   parameterization schemes are chosen according to sensitivity experiments, and the model
516   performance is also evaluated by observational data, there are inevitable uncertainties in the
517   modelled meteorological fields, which may directly affect the estimate of ABL-FT water
518   vapour exchange flux. For example, the difference between the simulated ABL height and the
519   observed value (~70 m and 120 m in winter and summer) brings ~30% uncertainty to the
520   acquisition of vertical velocity at this level, which may affect the accuracy of the flux results
521   in a similar magnitude. In addition, ignoring the turbulence term in this study may also reduce
522   the accuracy of the results. Nevertheless, this work presents a general view of long-term and
523   large-scale ABL-FT water vapour exchange over eastern China.
524   The water vapour exchange in the climatological sense presents a significant regional
525   division of north and south China, due to their quite distinct climatic features. In addition to
526   this general pattern, the spatial heterogeneity associated with the topographic distribution is
527   also noteworthy. We try to sort out the vertical exchange fluxes of water vapour over the ocean,
528   plain and mountain, roughly by the altitude below 0m, between 0-200m and greater than 200m.
529   The statistical results show that the ocean and plain are characterized by the upward output of
530   water vapour from the ABL, while the mountainous regions are dominated by downward
531   transport. This mode reflects the important role of the complex terrain in causing ABL-FT
532   vertical exchange. As described in Sect. 3.2, the prevailing airflow is obstructed by the
533   mountains to forcingly ascend on the windward and densely descend on the leeward slope, then
534   it decelerates and converges to induce upward motion when reaching the plain area. This
535   vertical motion pattern makes the water vapour upward export from the ABL in the plain, and
536   downward transport in mountainous areas due to the intensity and effect of the leeward side
537   subsidence being larger than that of the uplift in the windward side. For the ocean area,
538   horizontal wind crossing the inclined boundary layer top is responsible for the ABL water
539   vapour output, especially in the nearshore region. We admit the current analysis is preliminary,
540   but it does indicate the characteristics of vertical exchange flux distribution with topography,
541   and the significance of the interaction between mountain/sea and synoptic airflow. This finding
542   suggests that topographic ventilation is not only caused by mesoscale circulations such as
543   daytime upslope winds/sea breezes around mountains/coasts (Henne et al., 2004; Weigel et al.,

544 2007) or convective activities on a relatively small scale or a specific time (Gonzalez et al.,
545 2016; Dahinden et al., 2021). Dynamical forcing of terrain on seasonal airflow or synoptic
546 winds is more essential, which induces vertical motion and leads to systematic water vapour
547 exchange. The topographic-dependent feature of water vapour vertical exchange should also
548 be of general meaning to other complex terrain regions around the world.

549 Moreover, the climatology of water vapour exchange flux between ABL and FT provides
550 a quantitative background for investigating weather processes, radiation feedback and climate
551 changes. Water vapour entering the FT may provide more latent heat to the energy flows and
552 further affect synoptic systems. It is also involved in the radiative budget to influence climate.
553 Previous model simulations and observations indicate that small yet systematic changes in the
554 humidity of the upper atmosphere modulate the magnitude of the hydrological cycle and
555 radiative feedback, including clouds and precipitation (Minschwaner and Dessler, 2004;
556 Sherwood et al., 2010; Allan, 2012). Our results also demonstrate a notable relation between
557 precipitation anomalies and ABL-FT water vapour exchange patterns. Based on the
558 quantitative results in this study, the specific role of ABL - FT water vapour exchange in
559 Earth's energy flows and climate system might be studied further in the future.

4 Conclusions

561 In this study, we developed a climatology of water vapour exchange flux between the
562 ABL and FT, based on 7-year meteorological modelling data. The ABL water vapour
563 conservation method was used to estimate the vertical exchange flux across the ABL-FT
564 interface. Spatial distribution and seasonal characteristics of the water vapour exchange were
565 presented, and the influential mechanisms were analysed. The interannual difference was
566 simply discussed through its variations with ENSO events. The major findings of this work are
567 as follows:

568 (1) The spatiotemporal distribution of the ABL-FT water vapour exchange was
569 characterized by regional division and seasonal variation. During January and October in the
570 northern part (32-42°N), water vapour transport was downward to maintain ABL moisture,
571 while in the southern region (20-32°N) it was persistently exported to moisture the FT, with
572 the output flux from 10% to 80% of the surface evaporation rate.

573 (2) Vertical motion at the ABL-FT interface played a key role in the long-term (monthly
574 or seasonal) average state of water vapour vertical exchange, which was caused by the dynamic
575 forcing of the complex terrain on large-scale airflow. The temporal evolution of the vertical
576 exchange flux over the course of one day was primarily driven by the diurnal cycle of the ABL
577 height.

578 (3) Interannual variability of ABL-FT water vapour exchange was related to ENSO. Their
579 correlation was shown as a triple anti-phase distribution, with exchange strengthening in the
580 central zone and weakening in the north and south in La Niña years (and vice versa in El Niño
581 years). It was mainly attributed to the alteration of vertical velocity and water vapour content

582 at the ABL top varying with ENSO phases. Moreover, this pattern presented a good
583 correspondence to the distribution of precipitation anomalies.

584   This work is the first trial to quantitatively reveal the climatological state of ABL-FT
585 water vapour exchange flux over eastern China. Though for this specific research domain, the
586 method and results derived in the present study may provide reference to other regions of the
587 world. Through this study, the moisture linkage between the earth's surface and the upper layer
588 atmosphere is more clearly described. This may help us to obtain a better understanding of the
589 atmospheric water cycle.

Data availability

591 The data in this study are available from the corresponding author (xhcai@pku.edu.cn).

Author contribution

593 XHC and XPJ designed the research. LK and HSZ collected the data. XPJ performed the
594 simulations and wrote the paper. XHC reviewed and commented on the paper. QQH, YS, XSW
595 and TZ participated in the discussion of the article.

Competing interests

597 The authors declare that they have no conflict of interest.

Acknowledgements

599 This work was supported by National Key Research and Development Program of China
600 (2023YFC3706300, 2018YFC0213204).

References

602 Adebiyi, A. A., Zuidema, P., and Abel, S. J.: The Convolution of Dynamics and Moisture with
603   the Presence of Shortwave Absorbing Aerosols over the Southeast Atlantic, Journal of
604   Climate, 28, 1997-2024, doi:10.1175/jcli-d-14-00352.1, 2015.
605 Allan, R. P.: The Role of Water Vapour in Earth's Energy Flows, Surveys in Geophysics, 33,
606   557-564, doi:10.1007/s10712-011-9157-8, 2012.
607 Andrey, J., Cuevas, E., Parrondo, M. C., Alonso-Perez, S., Redondas, A., and Gil-Ojeda, M.:
608   Quantification of ozone reductions within the Saharan air layer through a 13-year
609   climatologic analysis of ozone profiles, Atmospheric Environment, 84, 28-34,
610   doi:10.1016/j.atmosenv.2013.11.030, 2014.

611 Bailey, A., Toohey, D., and Noone, D.: Characterizing moisture exchange between the
612   Hawaiian convective boundary layer and free troposphere using stable isotopes in water,
613   Journal of Geophysical Research-Atmospheres, 118, 8208-8221, doi:10.1002/jgrd.50639,
614   2013.

615 Boutle, I. A., Beare, R. J., Belcher, S. E., Brown, A. R., and Plant, R. S.: The Moist Boundary
616   Layer under a Mid-latitude Weather System, Boundary-Layer Meteorology, 134, 367-386,
617   doi:10.1007/s10546-009-9452-9, 2010.

618 Boutle, I. A., Belcher, S. E., and Plant, R. S.: Moisture transport in midlatitude cyclones,
619   Quarterly Journal of the Royal Meteorological Society, 137, 360-373, doi:10.1002/qj.783,
620   2011.

621 Chen, F., and Dudhia J.: Coupling an advanced land surface-hydrology model with the Penn
622   State-NCAR MM5 modeling system. Part I: Model implementation and sensitivity.
623   Monthly Weather Review, 129(4), 569-585, doi:10.1175/1520-
624   0493(2001)129<0569:caalsh>2.0.co, 2001.

625 Dacre, H. F., Gray, S. L., and Belcher, S. E.: A case study of boundary layer ventilation by
626   convection and coastal processes, Journal of Geophysical Research-Atmospheres, 112,
627   doi:10.1029/2006jd007984, 2007.

628 Dahinden, F., Aemisegger, F., Wernli, H., Schneider, M., Diekmann, C. J., Ertl, B., Knippertz,
629   P., Werner, M., and Pfahl, S.: Disentangling different moisture transport pathways over the
630   eastern subtropical North Atlantic using multi-platform isotope observations and high-
631   resolution numerical modelling, Atmospheric Chemistry and Physics, 21, 16319-16347,
632   doi:10.5194/acp-21-16319-2021, 2021.

633 Diaz, H. F. and Markgraf, V.: El Niño and the Southern Oscillation: Multiscale Variability and
634   Global and Regional Impacts, Cambridge University Press: Cambridge, UK, 496 pp., ISBN
635   0-521-621380-0, 2000.

636 Domroes, M. and Peng, G.: The Climate of China, Springer, Berlin, 361 pp., ISBN
637   3540187685, 1988.

638 Dudhia, J.: Numerical study of convection observed during the winter monsoon experiment
639   using a mesoscale two-dimensional model. Journal of Atmospheric Sciences, 46, 3077-
640   3107, doi:10.1175/1520-0469(1989)046<3077:nsocod>2.0.co;2, 1989.

641 Felix Correia Filho, W. L., de Oliveira-Junior, J. F., da Silva Junior, C. A., and Santiago, D. d.
642   B.: Influence of the El Nino-Southern Oscillation and the sypnotic systems on the rainfall
643   variability over the Brazilian Cerrado via Climate Hazard Group InfraRed Precipitation
644   with Station data, International Journal of Climatology, 42, 3308-3322,
645   doi:10.1002/joc.7417, 2022.

646 Fritz, C. and Wang, Z.: A Numerical Study of the Impacts of Dry Air on Tropical Cyclone
647   Formation: A Development Case and a Nondevelopment Case, Journal of the Atmospheric
648   Sciences, 70, 91-111, doi:10.1175/jas-d-12-018.1, 2013.

649   Gao, Y., Wang, H. J., and Chen, D: Precipitation anomalies in the Pan-Asian monsoon region
650   during El Niño decaying summer 2016, International Journal of Climatology, 38, 3618–
651   3632, doi:10.1002/joc.5522, 2018.

652   Ghannam, K., Duman, T., Salesky, S. T., Chamecki, M., and Katul, G.: The non-local character
653   of turbulence asymmetry in the convective atmospheric boundary layer, Quarterly Journal
654   of the Royal Meteorological Society, 143, 494-507, doi:10.1002/qj.2937, 2017.

655   Gonzalez, A., Exposito, F. J., Perez, J. C., Diaz, J. P., and Taima, D.: Verification of
656   precipitable water vapour in high-resolution WRF simulations over a mountainous
657   archipelago, Quarterly Journal of the Royal Meteorological Society, 139, 2119-2133,
658   doi:10.1002/qj.2092, 2013.

659   Gonzalez, Y., Schneider, M., Dyroff, C., Rodriguez, S., Christner, E., Elena Garcia, O.,
660   Cuevas, E., Jose Bustos, J., Ramos, R., Guirado-Fuentes, C., Barthlott, S., Wiegele, A., and
661   Sepulveda, E.: Detecting moisture transport pathways to the subtropical North Atlantic free
662   troposphere using paired H2O-delta D in situ measurements, Atmospheric Chemistry and
663   Physics, 16, 4251-4269, doi:10.5194/acp-16-4251-2016, 2016.

664   Grell, G. A., and Devenyi, D.: A generalized approach to parameterizing convection combining
665   ensemble and data assimilation techniques, Geophysical Research Letters, 29,
666   doi:10.1029/2002gl015311, 2002.

667   Gvozdikova, B. and Mueller, M.: Moisture fluxes conducive to central European extreme
668   precipitation events, Atmospheric Research, 248, doi:10.1016/j.atmosres.2020.105182,
669   2021.

670   Hagos, S. M. and Cook, K. H.: Dynamics of the West African monsoon jump, Journal of
671   Climate, 20, 5264-5284, doi:10.1175/2007jcli1533.1, 2007.

672   Harries, J., Carli, B., Rizzi, R., Serio, C., Mlynczak, M., Palchetti, L., Maestri, T., Brindley,
673   H., and Masiello, G.: The far-infrared Earth, Reviews of Geophysics, 46,
674   doi:10.1029/2007rg000233, 2008.

675   Henne, S., Furger, M., and Prevot, A. S. H.: Climatology of mountain venting-induced elevated
676   moisture layers in the lee of the Alps, Journal of Applied Meteorology, 44, 620-633,
677   doi:10.1175/jam2217.1, 2005.

678   Hersbach, H., Bell, B., Berrisford, P., Biavati, G., Horányi, A., Muñoz Sabater, J., Nicolas, J.,
679   Peubey, C., Radu, R., Rozum, I., Schepers, D., Simmons, A., Soci, C., Dee, D., and
680   Thépaut, J. N.: ERA5 hourly data on pressure levels from 1940 to present. Copernicus
681   Climate Change Service (C3S) Climate Data Store (CDS), doi: 10.24381/cds.bd0915c6,
682   2023.

683   Hirota, N., Ogura, T., Tatebe, H., Shiogama, H., Kimoto, M., and Watanabe, M.: Roles of
684   Shallow Convective Moistening in the Eastward Propagation of the MJO in MIROC6,
685   Journal of Climate, 31, 3033-3047, doi:10.1175/jcli-d-17-0246.1, 2018.

686   Hong, S. Y., and Lim, J. J.: The WRF single-moment 6-class microphysics scheme (WSM6),
687   Journal of Korean Meteorological Society, 42, 129-151, 2006.

688 Hong, S. Y., Noh, Y., and Dudhia, J.: A new vertical diffusion package with an explicit
689   treatment of entrainment processes, Monthly Weather Review, 134, 2318-2341,
690   doi:10.1175/mwr3199.1, 2006.

691 Hov, O., and Flatoy, F.: Convective redistribution of ozone and oxides of nitrogen in the
692   troposphere over Europe in summer and fall. Journal of Atmospheric Chemistry, 28, 319-
693   337, doi:10.1023/a:1005780730600, 1997.

694 Jain, S., and Kar, S. C.: Transport of water vapour over the Tibetan Plateau as inferred from
695   the model simulations, Journal of Atmospheric and Solar-Terrestrial Physics, 161, 64-75,
696   doi:10.1016/j.jastp.2017.06.016, 2017.

697 Jin, X. P., Cai, X. H., Huang, Q. Q., Wang, X. S., Song, Y., and Zhu, T.: Atmospheric Boundary
698   Layer-Free Troposphere Air Exchange in the North China Plain and its Impact on PM2.5
699   Pollution, Journal of Geophysical Research-Atmospheres, 126,
700   doi:10.1029/2021jd034641, 2021.

701 Jin, X. P., Cai, X. H., Yu, M. Y., Song, Y., Wang, X. S., Kang, L., and Zhang, H. S.: Diagnostic
702   analysis of wintertime PM2.5 pollution in the North China Plain: The impacts of regional
703   transport and atmospheric boundary layer variation, Atmospheric Environment, 224,
704   doi:10.1016/j.atmosenv.2020.117346, 2020.

705 Kain, J. S.: The Kain-Fritsch convective parameterization: An update, Journal of Applied
706   Meteorology, 43, 170-181, doi:10.1175/1520-0450(2004)043<0170:tkcpau>2.0.co;2,
707   2004.

708 Kiehl, J. T., and Trenberth, K. E.: Earth's annual global mean energy budget, Bulletin Of The
709   American Meteorological Society, 78, 197-208, doi:10.1175/1520-
710   0477(1997)078<0197:eagmeb>2.0.co;2, 1997.

711 Knippertz, P. and Wernli, H.: A Lagrangian Climatology of Tropical Moisture Exports to the
712   Northern Hemispheric Extratropics, Journal of Climate, 23, 987-1003,
713   doi:10.1175/2009jcli3333.1, 2010.

714 Kossmann, M., Corsmeier, U., de Wekker, S. F. J., Fiedler, F., Vogtlin, R., Kalthoff, N.,
715   Gusten, H. and Neininger, B.: Observations of handover processes between the atmospheric
716   boundary layer and the free troposphere over mountainous terrain. Contributions to
717   Atmospheric Physics, 72, 329-350, 1999.

718 Kousky, V. E., Kagano, M. T., and Cavalcanti, I. F. A.: A review of the southern oscillation-
719   oceanic-atmospheric circulation changes and related rainfall anomalies, Tellus Series A,
720   36, 490-504, doi:10.1111/j.1600-0870.1984.tb00264.x, 1984.

721 Li, Q. H., Wu, B. G., Liu, J. L., Zhang, H. S., Cai, X. H., and Song, Y.: Characteristics of the
722   atmospheric boundary layer and its relation with PM2.5 during haze episodes in winter in
723   the North China Plain, Atmospheric Environment, 223,
724   doi:10.1016/j.atmosenv.2020.117265, 2020.

725 Lin, Y. L., Farley, R. D., and Orville, H. D.: Bulk parameterization of the snow field in a cloud
726   model. Journal of Climate Applied Meteorology, 22, 1065-1092, doi:10.1175/1520-
727   0450(1983)022<1065:bpotsf>2.0.co;2, 1983.

Liu, B., Tan, X., Gan, T. Y., Chen, X., Lin, K., Lu, M., and Liu, Z.: Global atmospheric moisture transport associated with precipitation extremes: Mechanisms and climate change impacts, Wiley Interdisciplinary Reviews-Water, 7, 10.1002/wat2.1412, 2020.

Liu, S. Y., and Liang, X. Z.: Observed Diurnal Cycle Climatology of Planetary Boundary Layer Height, Journal of Climate, 23, 5790-5809, doi:10.1175/2010jcli3552.1, 2010.

Marchukova, O. V., Voskresenskaya, E. N., and Lubkov, A. S.: Diagnostics of the La Niña events in 1900–2018, Earth Environmental Sciences, 606, 012036, doi:10.1088/1755-1315/606/1/012036, 2020.

McKendry, I. G., and Lundgren, J.: Tropospheric layering of ozone in regions of urbanized complex and/or coastal terrain: a review, Progress in Physical Geography, 24, 329-354, doi: 10.1177/030913330002400302, 2000.

Minschwaner, K., and Dessler, A. E.: Water vapor feedback in the tropical upper troposphere: model results and observations. Journal of Climate, 17, 1272-1282, doi:10.1175/1520-0442(2004)017<1272:WVFITT>2.0.CO;2, 2004.

Miura, H., Satoh, M., Tomita, H., Noda, A. T., Nasuno, T., and Iga, S.-i.: A short-duration global cloud-resolving simulation with a realistic land and sea distribution, Geophysical Research Letters, 34, doi:10.1029/2006gl027448, 2007.

Mlawer, E. J., Taubman, S. J., Brown, P. D., Iacono, M. J., and Clough, S. A.: Radiative transfer for inhomogeneous atmospheres: RRTM, a validated correlated-k model for the longwave, Journal of Geophysical Research: Atmospheres, 102, 16663-16682, doi:10.1029/97jd00237, 1997.

Newell, R. E., Zhu, Y., and Scott, C.: Tropospheric rivers-a pilot-study, Geophysical Research Letters, 19, 2401-2404, doi:10.1029/92gl02916, 1992.

Perez, J. C., Garcia-Lorenzo, B., Diaz, J. P., Gonzalez, A., Exposito, F., and Insausti, M.: Forecasting precipitable water vapor at the Roque de los Muchachos Observatory, Conference on Ground-Based and Airborne Telescopes III, San Diego, CA, 2010 Jun 27-Jul 02, WOS:000285506700149, doi:10.1117/12.859453, 2010.

Pilinis, C., Seinfeld, J. H., and Grosjean, D.: Water-content of atmospheric aerosols, Atmospheric Environment, 23, 1601-1606, doi:10.1016/0004-6981(89)90419-8, 1989.

Qian, X., Yao, Y. Q., Wang, H. S., Zou, L., Li, Y., and Yin, J.: Validation of the WRF Model for Estimating Precipitable Water Vapor at the Ali Observatory on the Tibetan Plateau, Publications of the Astronomical Society of the Pacific, 132, doi:10.1088/1538-3873/abc22d, 2020.

Sherwood, S. C., Roca, R., Weckwerth, T. M., and Andronova, N. G.: Tropospheric water vaporm convection, and climate, Reviews of Geophysics, 48, doi:10.1029/2009rg000301, 2010.

Sherwood, S. C.: Maintenance of the free-tropospheric tropical water vapor distribution 1. Clear regime budget, Journal of Climate, 9, 2903-2918, doi:10.1175/1520-0442(1996)009<2903:motftt>2.0.co;2, 1996.

767 Sinclair, V. A., Belcher, S. E., and Gray, S. L.: Synoptic Controls on Boundary-Layer
768   Characteristics, Boundary-Layer Meteorology, 134, 387-409, doi:10.1007/s10546-009-
769   9455-6, 2010.

770 Sodemann, H. and Stohl, A.: Moisture Origin and Meridional Transport in Atmospheric Rivers
771   and Their Association with Multiple Cyclones, Monthly Weather Review, 141, 2850-2868,
772   doi:10.1175/mwr-d-12-00256.1, 2013.

773 Stull, R. B.: An Introduction to Boundary Layer Meteorology. Kluwer Acad., Dordrecht,
774   Netherlands, 670 pp, doi:10.1007/978-94-009-3027-8, 1988.

775 Sun, L., Shen, B. Z., and Sui, B.: A Study on Water Vapor Transport and Budget of Heavy
776   Rain in Northeast China, Advances in Atmospheric Sciences, 27, 1399-1414,
777   doi:10.1007/s00376-010-9087-2, 2010.

778 Tabazadeh, A., Santee, M. L., Danilin, M. Y., Pumphrey, H. C., Newman, P. A., Hamill, P. J.,
779   and Mergenthaler, J. L.: Quantifying denitrification and its effect on ozone recovery,
780   Science, 288, 1407-1411, doi:10.1126/science.288.5470.1407, 2000.

781 van Dop, H., and Verver, G.: Countergradient transport revisited, Journal of Atmospheric
782   Sciences, 58, 2240-2247, doi: 10.1175/1520-0469(2001)058<2240:CTR>2.0.CO;2, 2001.

783 Walker, G. T., and Bliss, E. W.: World weather V., Memoirs of the Royal Meteorological
784   Society, 4, 53-84, 1932.

785 Walker, G. T., and Bliss, E. W.: World weather VI., Memoirs of the Royal Meteorological
786   Society, 4, 119-139, 1937.

787 Wang, L. J., Cai, C., and Zhang, H. Y.: Circulation characteristics and critical systems of
788   summer precipitation in eastern China under the background of two types of ENSO events,
789   Transactions of Atmospheric Sciences, 43, 617-629,
790   doi:10.13878/j.cnki.dqkxxb.20180817002, 2020.

791 Weigel, A. P., Chow, F. K., and Rotach, M. W.: The effect of mountainous topography on
792   moisture exchange between the "surface" and the free atmosphere, Boundary-Layer
793   Meteorology, 125, 227-244, doi:10.1007/s10546-006-9120-2, 2007.

794 Wolter, K. and Timlin, M. S.: El Nino/Southern Oscillation behaviour since 1871 as diagnosed
795   in an extended multivariate ENSO index (MEI.ext), International Journal of Climatology,
796   31, 1074-1087, doi:10.1002/joc.2336, 2011.

797 Wong, S., Naud, C. M., Kahn, B. H., Wu, L., and Fetzer, E. J.: Coupling of Precipitation and
798   Cloud Structures in Oceanic Extratropical Cyclones to Large-Scale Moisture Flux
799   Convergence, Journal of Climate, 31, 9565-9584, doi:10.1175/jcli-d-18-0115.1, 2018.

800 Wu, J. R., Bei, N. F., Hu, B., Liu, S. X., Zhou, M., Wang, Q. Y., Li, X., Liu, L., Feng, T., Liu,
801   Z. R., Wang, Y. C., Cao, J. J., Tie, X. X., Wang, J., Molina, L. T., and Li, G. H.: Is water
802   vapour a key player of the wintertime haze in North China Plain?, Atmospheric Chemistry
803   and Physics, 19, 8721-8739, doi:10.5194/acp-19-8721-2019, 2019.

804 Wypych, A., Bochenek, B., and Rozycki, M.: Atmospheric Moisture Content over Europe and
805   the Northern Atlantic, Atmosphere, 9, doi:10.3390/atmos9010018, 2018.

806 Xue, F., Zeng, Q. C., Huang, R. H., Li, C. Y., Lu, R. Y., Zhou, T. J.: Recent Advances in
807   Monsoon Studies in China, Advances in Atmospheric Sciences, 32, 206-229,
808   doi:10.1007/s00376-014-0015-8, 2015.

809 You, T., Wu, R. G., Liu, G., and Chai, Z. Y.: Contribution of precipitation events with different
810   consecutive days to rainfall change over Asia during ENSO years, Theoretical and Applied
811   Climatology, 144, 147-161, doi:10.1007/s00704-021-03538-8, 2021.

812 Zhang, H. G., Hu, Y. T., Cai, J. D., Li, X. J., Tian, B. H., Zhang, Q. D., and An, W.: Calculation
813   of evapotranspiration in different climatic zones combining the long-term monitoring data
814   with bootstrap method, Environmental Research, 191, doi:10.1016/j.envres.2020.110200,
815   2020.

816 Zheng, J., Bian, J., Ge, Q., Hao, Z., Yin, Y., and Liao Y.: The climate regionalization in China
817   for 1981-2010, Chinese Science Bulletin, 58, 3088-3099, doi:10.1360/972012-1491, 2013.

818 Zhou, T. J., and Yu, R. C.: Atmospheric water vapor transport associated with typical
819   anomalous summer rainfall patterns in China, Journal of Geophysical Research-
820   Atmospheres, 110, doi:10.1029/2004jd005413, 2005.

821 Zhou, W., Chen, W., and Wang, D. X.: The implications of El Niño-Southern Oscillation signal
822   for South China monsoon climate, Aquatic Ecosystem Health & Management, 15, 14–19,
823   doi:10.1080/14634988.2012.652050, 2012.

824 Zhu, Y., and Newell, R. E.: A proposed algorithm for moisture fluxes from atmospheric rivers,
825   Monthly Weather Review, 126, 725-735, doi:10.1175/1520-
826   0493(1998)126<0725:apafmf>2.0.co;2, 1998.